# 3D TEM Tomography of Templated Bilayer Films of Block Copolymers

*Kevin W. Gotrik, Thomas Lam, Adam F. Hannon, Wubin Bai, Yi Ding, Jonathan Winterstein, Alfredo Alexander-Katz, J. Alexander Liddle, and Caroline A. Ross**

**Transmission electron microscope (TEM) tomography was used to visualize the morphology and 3D connectivity of a lithographically templated, self-assembled bilayer film of cylinder-forming 45.5 kg/mol polystyrene-*block*-polydimethylsiloxane. The structure, formed after a 5 min solvothermal anneal, was imaged with a resolution of ≈3 nm in 3D, enabling a comparison between measurement and self-consistent mean-field theory (SCFT) calculations. Images of etched and unetched samples showed that etching collapsed the PDMS microdomain structure and reduced the template dimensions. In addition to the general comparison between modeled and measured dimensions, the tomography revealed connections between the orthogonal layers of cylinders at their crossing points. Comparison with the SCFT model, even under solvothermal annealing conditions, shows that it is helpful in understanding the detailed nanoscale structure of features created by directed self-assembly (DSA), which is essential in developing nanomanufacturing processes based on DSA.**

## 1. Introduction

Current photolithographic tools, operating at a wavelength of 193 nm, are limited in their ability to produce small (< 30 nm) features at dense pitches.[1] This has led in recent years, to the adoption of a variety of double, triple, or even quadruple patterning approaches that have eroded the traditional cost-effectiveness of photolithography. Block copolymer (BCP) directed self-assembly (DSA) employs relatively sparse chemical or topographical lithographic features to template the periodic microdomain features of the BCP, enabling the patterning of high-resolution features and maintaining the requisite pattern-placement accuracy for advanced integrated circuit manufacture.[2–7] BCPs enjoy a flexibility in chemistry and they can be tuned for many applications, such as hard masks for bit patterned media,[8] filtration membranes,[9,10] electrolytes with high Li-ion conductivity,[11,12] and nanowire[13] or nanoparticle[14] growth templates.

In order for BCP DSA to be used successfully in integrated circuit manufacturing, it is essential that validated models and design tools are available that can be used to predict the BCP features that will be generated from a given template.[15] Self-consistent field theory (SCFT) has been used extensively to model the behavior of BCPs, and has been compared with transmission electron microscopy (TEM) or scanning electron microscopy (SEM) images for thin films and for BCPs confined in cylindrical or spherical pores.[16] 3D TEM tomography has been applied to image microdomains in a range of bulk BCPs[17–19] and even to study the effects of confinement, solvent evaporation rate and nanoparticle incorporation.[20–25] However, real-space tomography measurements of BCP morphologies formed by directed self-assembly, where the templating structures and substrate are still intact, and the images are of sufficient quality to enable model validation, have not previously been carried out. Soft X-ray scattering experiments and grazing incidence X-ray scattering (GISAXS) have recently enabled some direct quantitative structure comparison with simulations for thin film lamellar systems, but these methods are still indirect and require the scattering data to be converted to the real space structure profiles through computational methods.[26,27] In addition, such scattering methods generate ensemble measurement data and are therefore insensitive to the presence of small defect populations. In integrated circuit fabrication in particular, understanding the form and origin of such defects is essential.[28]

Here we use TEM tomography to generate high-resolution, three-dimensional reconstructions of a solvothermal-annealed BCP that has undergone directed self-assembly on a template consisting of posts,[29] and compare the results with SCFT[29–33] calculations of the 3D microdomain structure as well as with the microdomain structure revealed by etching away the majority block. A polystyrene-*block*-polydimethylsiloxane (PS-*b*-PDMS) diblock copolymer was selected for this study because the Si content of the PDMS provides sufficient mass and phase

K. W. Gotrik,[+] A. F. Hannon, W. Bai, Y. Ding, A. Alexander-Katz, C. A. Ross
Department of Materials Science and Engineering
Massachusetts Institute of Technology
77 Massachusetts Avenue
Cambridge, Massachusetts 02139
E-mail: caross@mit.edu
T. Lam,[+] J. Winterstein, J. A. Liddle
Center for Nanoscale Science and Technology
National Institute of Standards and Technology
100 Bureau Drive, Gaithersburg, Maryland 20899
[+]These authors contributed equally to this work

**DOI: 10.1002/adfm.201402457**

contrast to enable the phases to be distinguished under conventional bright-field imaging conditions, without staining or etching. The contrast can be further enhanced by defocusing to a degree at which image processing techniques can be used to automatically identify the boundaries of the two microdomains. Although the defocus degrades the resolution, at an accelerating voltage of 200 kV, and with typical defocus values of up to 3.5 µm (necessary to yield adequate contrast), a resolution of at least 3 nm can still be achieved.[34] This is comparable to the resolution of the SCFT model used here, which has a coarse-graining length scale of 2.6 nm (see Supporting Information (SI)).

Previous TEM tomography studies[17,18] examined the morphology of bulk block copolymer systems using samples prepared by ultramicrotomy or direct casting of thin films. Ideally, samples for TEM tomography would be in the form of cylinders to enable tilting through an angular range of ± 90°. However, in the case of a 40 nm thick BCP film on a lithographically patterned substrate, this is not possible, and the tilting range is reduced, leading to the formation of so-called "missing wedge" artifacts.[35] In this study, we directly fabricated samples on an electron transparent $Si_3N_4$ support film designed for TEM tomography. Accounting for elongation errors, we examine the agreement between the 3D tomographic measurements and the SCFT model, serving to validate the model and to reveal details of the morphology of the two ordered layers of orthogonal cylinders: in particular the existence of connections between cylinders at the crosspoints. Furthermore, we used reactive ion etching (RIE) to treat the sample and compare pre- and post-processed tomographic data with data obtained by conventional SEM. We were not only able to assess the degree to which RIE changes the structure of the PDMS microdomains, but were also able to determine whether conventional, two-dimensional imaging provides a useful representation of these complex, three-dimensional structures.

The SCFT method is described in the SI and in previous studies.[29] The system was modeled using periodic boundary conditions with dimensions and geometry that reflect those encountered in the experiment. To account for the solvent annealing process, the film was treated as being swelled by solvent, with an effective volume fraction of PDMS, and a Flory-Huggins interaction parameter dependent upon the ratio of solvents used in the annealing. Additionally, this polymer has a high $\chi$ parameter, usually cited as 0.26[36,37] but recently calculated to be ≈ 0.14 at room temperature.[38] This means that during the solvent annealing process used here, the BCP is still below its order-disorder transition temperature and equilibrium microphase separation therefore occurs during the solvent annealing itself rather than during the quench from a disordered state.[27] It is therefore reasonable to carry out SCFT simulations of microphase separation by using an effective $\chi$ to include the solvent, rather than by modeling the solvent explicitly.[39] Unlike our prior work which included a range of post periods,[29] here we focus on a single post period but vary post height, effective $\chi$, and effective volume fraction in the model.

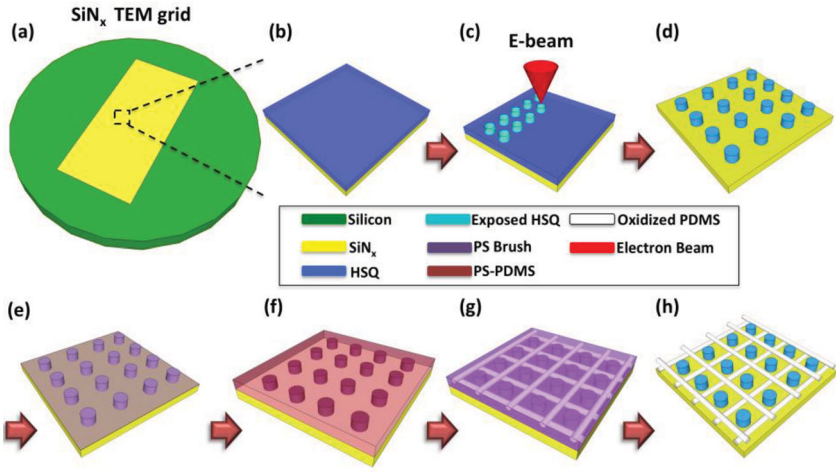


**Figure 1.** Schematic of the sample fabrication. a) $SiN_x$ TEM grid, b) spin coat HSQ resist, c) electron beam lithography to expose the array of posts, d) salty development of HSQ, e) polystyrene brush treatment of posts and substrate, f) spin coat PS-*b*-PDMS block copolymer, g) solvothermal annealing to produce in-plane cylindrical PDMS microdomains in a PS matrix, h) reactive ion etching to remove the PDMS surface layer then the PS matrix. TEM tomography is carried out at steps (g) and (h).

## 2. Results and Discussion

**Figure 1** is a flow diagram showing the process for preparing samples. Details of the methods, as well as the TEM tomography procedure, are given in the Experimental Section. The template was prepared by electron beam lithography and development of hydrogen silsesquioxane (HSQ) resist, spin-coated on a nitride membrane, to form an array of HSQ posts. This was spin-coated with PS-*b*-PDMS to a thickness of 32 nm, then followed by a solvothermal anneal to induce microphase separation.

**Figure 2** shows (a,b) TEM and (c,d) SEM images of the self-assembled microdomains before (a) and after (b-d) reactive ion etching to remove the PDMS surface layer then remove the PS matrix and oxidize the internal PDMS microdomains. In Figure 2(a), an image of the unetched templated film, the darkest circular features are the HSQ posts, seen from the top. Between each row of posts is a dark line indicating the presence of a PDMS cylinder. The cylinders running left to right are most clearly seen, but an orthogonal set running from top to bottom is also visible. Figure 2(b) shows a different region of the sample after oxygen RIE, which removed the PS, enhancing the contrast of the cylinders. The majority of the image showed orthogonal cylinders, but in some regions cylinder curvature and junctions are visible.

3D reconstructions and visualizations were performed in the dashed inset regions in Figure 2 (a,b). In the SI, the video S1 is of the reconstructed image stack (before the image stack was aligned for quantification) moving from top surface into the substrate plane of the unetched film. Figure 2(c) and (d) show top view and tilted SEM images respectively of an etched sample

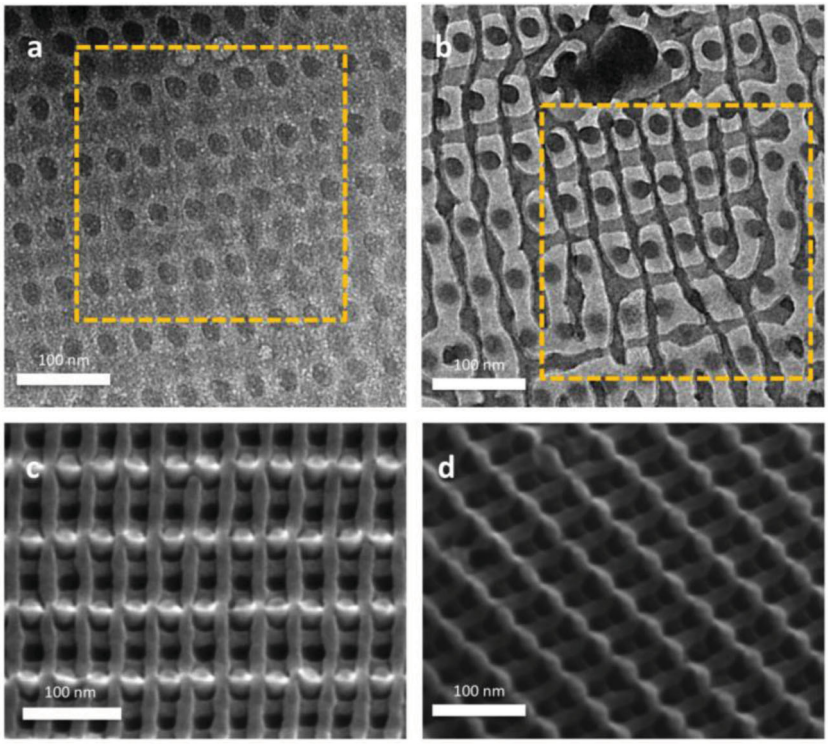


**Figure 2.** TEM of a) unetched sample and b) after oxygen etch. c) Top view and d) tilted view SEM images of another sample after RIE, made on an oxidized Si substrate using a similar process but with post spacing $d_x = 36$ nm, $d_y = 62$ nm.

prepared in a similar manner to give a sense of the topography of the oxidized PDMS after etching. From the etched sample it is difficult to determine the relationship between the top and bottom cylinders before etching, for example to determine the presence or absence of junctions between cylinders.

**Figure 3** shows the 3D visualization of the unetched sample (Figure 3(a)) and for comparison a visualization of the etched sample (Figure 3(b)). Figure 3a has been labeled so that posts and cylinders can be identified. Videos S2 and S3 in the SI are 3D tomography videos of unetched and etched structures respectively. From the TEM tomography a post spacing of $d_x = 34$ nm, $d_y = 65$ nm was measured in the unetched sample. It is clear that over the majority of the sample, the mesh of orthogonal cylinders formed interconnections at the crossing points. In the bottom left corner a third layer of cylinders started to form, and the cylinders between rows of posts X4 and X6 had discontinuous diameters.

From the analysis of the 3D visualized features of the unetched sample, quantitative statistics are presented in **Figure 4**. Within this region of the film a thickness gradient is present, shown by the contour plot in Figure 4(a), such that the left hand side had a thickness > 31 nm and the right hand side was < 29 nm. A gradient is also present in HSQ post height $h_p$, shown in the contour plot in Figure 4(b). So that the results can be compared with SCFT modeling, the HSQ post heights were expressed as $\frac{h_p}{L_0}$, where $L_0$ is the equilibrium cylinder period for the film on a smooth substrate, approximately 36 nm. The

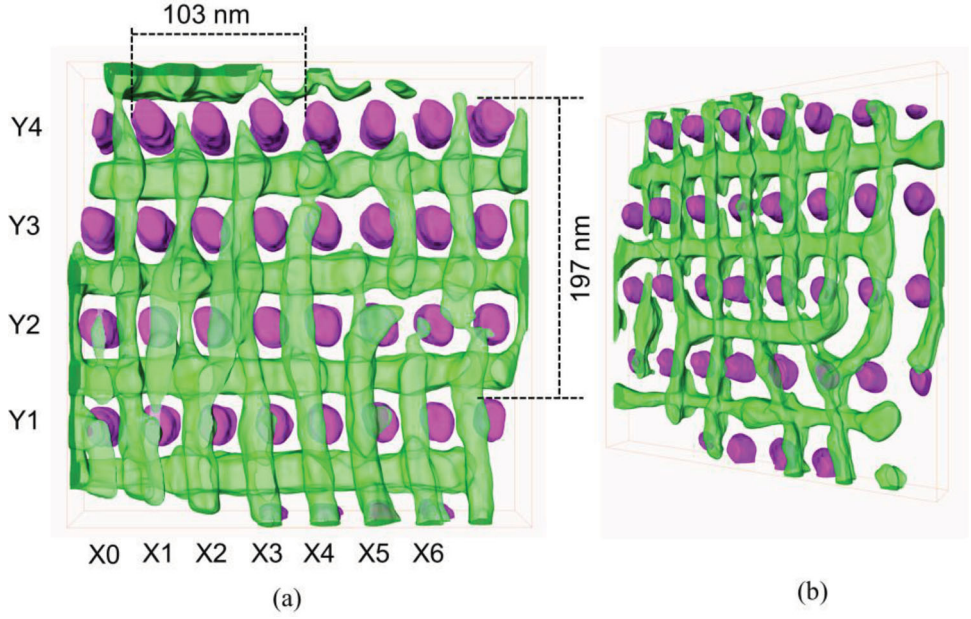


**Figure 3.** a) 3D visualization of the unetched structure and annotation of columns of HSQ posts marked X, and rows of HSQ posts marked Y with a bounding box volume of 296 nm × 296 nm × 40 nm. (Top-down view) b) Structure after etching, with a bounding box volume of 296 nm × 296 nm × 30 nm (tilted view). PDMS cylinders are presented in lighter transparent green and HSQ in purple.

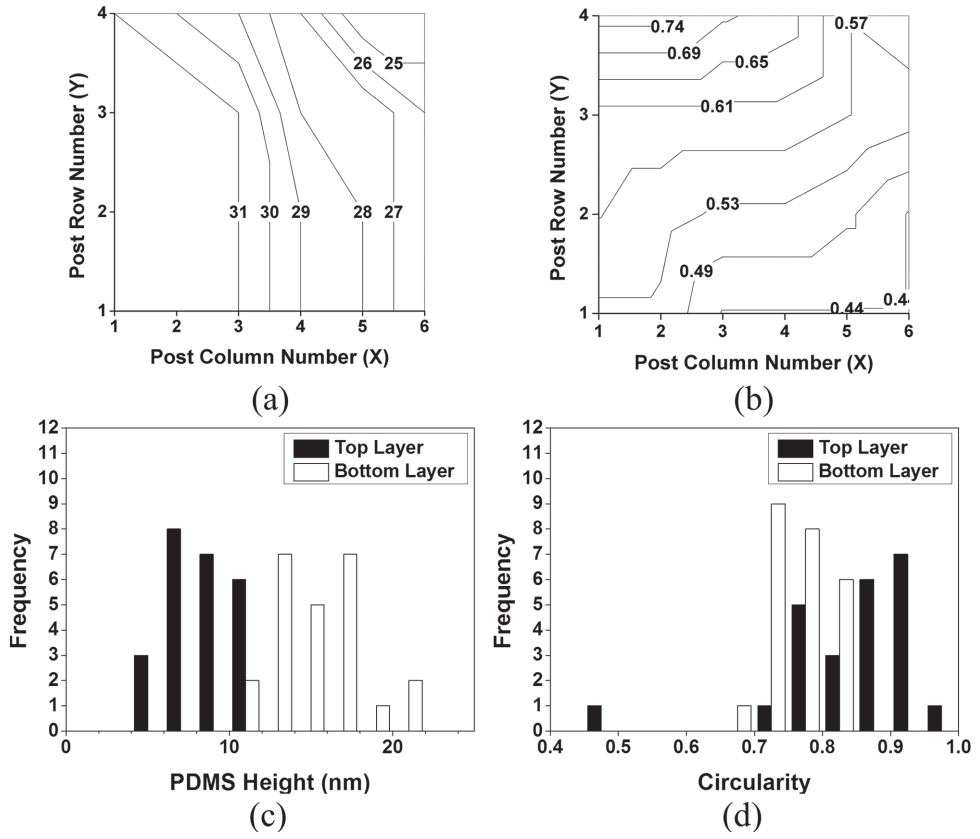


**Figure 4.** Quantitative measurements from TEM tomography. a) Contour plot of the total thickness of the PS-*b*-PDMS film, where the contour lines are in units of nm. The axes represent the position within the sample area indexed with respect to the rows and columns of posts. b) HSQ post heights plotted as $\frac{h_p}{L_0}$ at different positions within the sample area. c) Histogram of PDMS cylinder heights measured in the out of plane direction for top and bottom layers. d) Histogram of PDMS circularity for top and bottom layers.

average diameter of the HSQ posts was (20 ± 1) nm with a measured circularity of 0.86 ± 0.01, the tabulated statistics of which can be found in Table SI in the SI. Circularity is defined as $4\pi$[area]/[perimeter]$^2$ = 1 for a circle and < 1 for an ellipse. Unless noted otherwise all measurement uncertainties are quoted as (average ± one standard deviation).

Tomography revealed differences between the top and bottom layers of PDMS cylinders. PDMS cylinders in the bottom layer were thicker in the direction perpendicular to the substrate plane, with a peak in the distribution of cylinder diameters at 14 nm and 16 nm, in comparison to the top layer of cylinders with peak at 8 nm, Figure 4(c). The bottom-layer PDMS cylinders were also less circular in cross-section with many measurements of circularity between 0.75 and 0.85 and the major axis parallel to the film plane, whereas the top layer cylinders had circularity > 0.85 (Figure 4(d)). (Measurements of circularity were not corrected for elongation.) Tables SII-SIV of the tabulated statistics used to generate Figure 4 (b-d) can be found in the SI.

We now compare these findings to the results of the SCFT modeling. In solvent annealing the exact values for $\chi N$ and $f$ are not known *a priori* so a range of values was chosen for simulation. The $\chi N$ values chosen were 18, 24 and 30 which are below those predicted for the neat block copolymer, which has a lower limit of $\chi N = 68$ based on $\chi = 0.14$[38] and an upper limit of $\chi N = 126$ based on $\chi = 0.26$[36,37] with $N = 486$. The model uses a smaller $\chi N$ than for the neat BCP due to both the coarse-graining of the model, which includes only 125 segments per chain instead of 486, and the incorporation of solvent, which lowers $\chi$ by an amount proportional to the fraction of polymer volume. Similarly a range of $f = 0.32$ and 0.36 was modeled to account for a range of solvent selectivity.[27]

In addition to the $f$ and $\chi N$ explored in the model, three different substrate functionalizations were considered: top (air) surface and bottom (substrate) surface neutral to the two blocks; top surface preferential to PDMS and bottom surface neutral; and top surface preferential to PDMS and bottom surface preferential to PS. The posts themselves were always preferential to PS in the model. The model considered a BCP film thickness that would be commensurate with the formation of two layers of cylinders within the film, i.e., for the three different substrate functionalizations the modeled thickness was taken to be $2L_0$, $2.5L_0$ and $3L_0$ respectively.

**Figure 5** summarizes the morphologies predicted from SCFT. Fifteen distinct internal microdomain morphologies (neglecting the presence of surface and interface wetting layers) were identified within the range of parameters studied here, and are labeled and color coded in Figure 5a-l. Of interest, the dark blue, Figure 5h, represents cross-point structures where the upper and lower cylinders are connected at a junction.

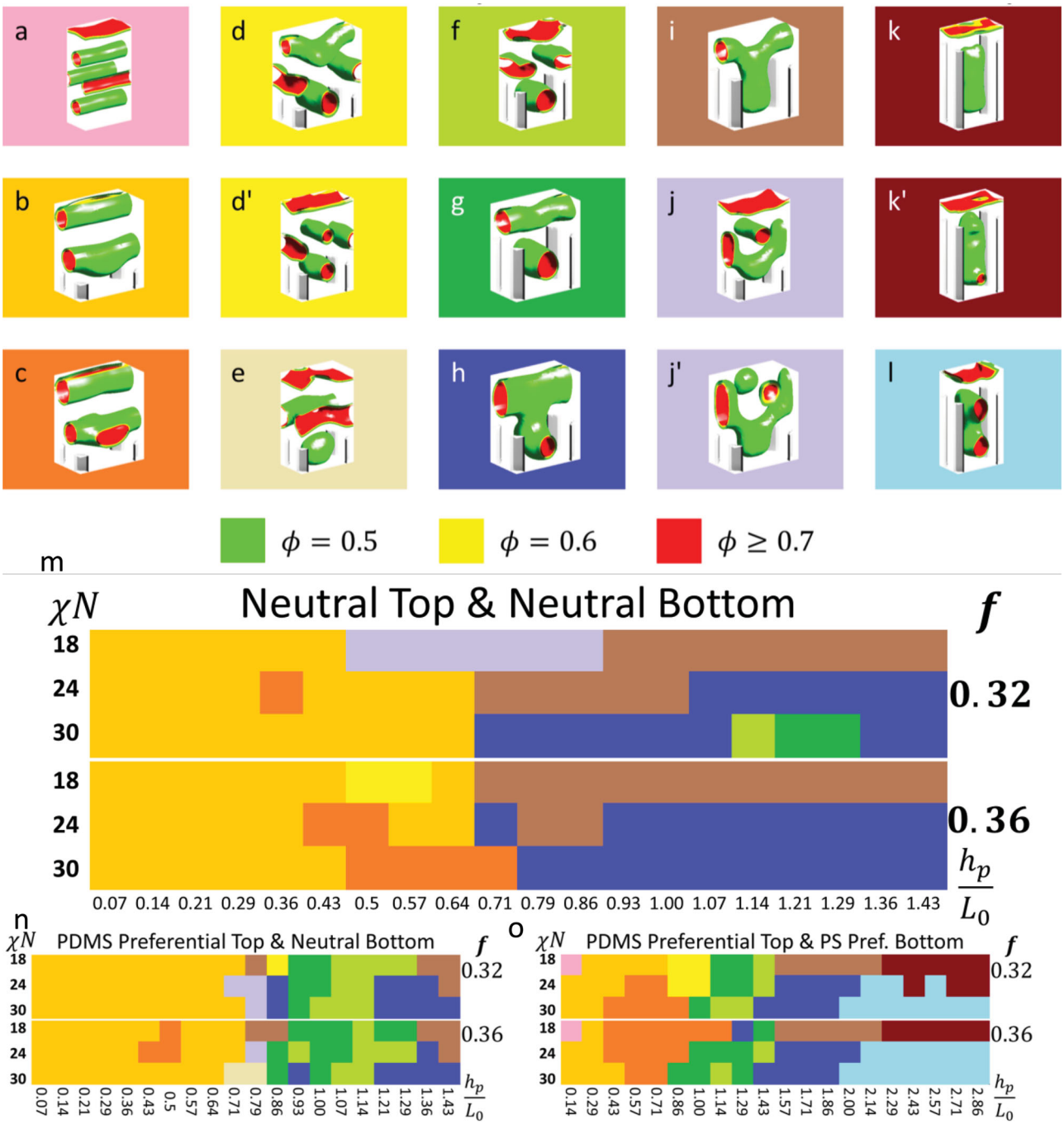


**Figure 5.** The morphologies found for a range of post heights, volume fractions and $\chi$N were a) triple layers of cylinders, b) double layers of cylinders/lamellae, c) cylinder over perforated lamellae, d) mesh single cylinder over double layer of cylinders or d') triple layer of cylinders, e) cylinder over sphere, f) double layer parallel cylinders, g) mesh structure (no connection), h) mesh structure (connected), i) cylinder with perpendicular cylinder, j) flipped mesh structure (not connected) or j') sphere over curved cylindrical structure, k) perpendicular cylinder or k') perpendicular cylinder with bottom connection, and l) double connected structure. Simulation cells are different heights, depending on the surface wetting condition. m,n,o) Phase diagrams showing the morphologies predicted under different boundary conditions. The colors correspond to the morphologies shown in (a–l), with dark blue representing the connected mesh structure. The phase diagrams were calculated as a function of normalized post height $\frac{h_p}{L_0}$ for f = 0.32 and 0.36, $\chi N$ = 18, 24 and 30, and three different surface wetting conditions: m) neutral top and bottom surfaces, n) minority preferential top surface, neutral bottom surface, o) minority preferential top surface, majority preferential bottom surface. The posts were always majority-preferential. o) shows a wider range of post heights than (m,n).

This is the actual morphology found over much of the sample. Figure 5m,n,o show a summary of which morphology is predicted for each of the three different substrate functionalizations over a range of post heights. The colors in Figure 5m,n,o match those of the different morphologies in Figure 5a-l. More detailed compilations of the results are given in the SI.

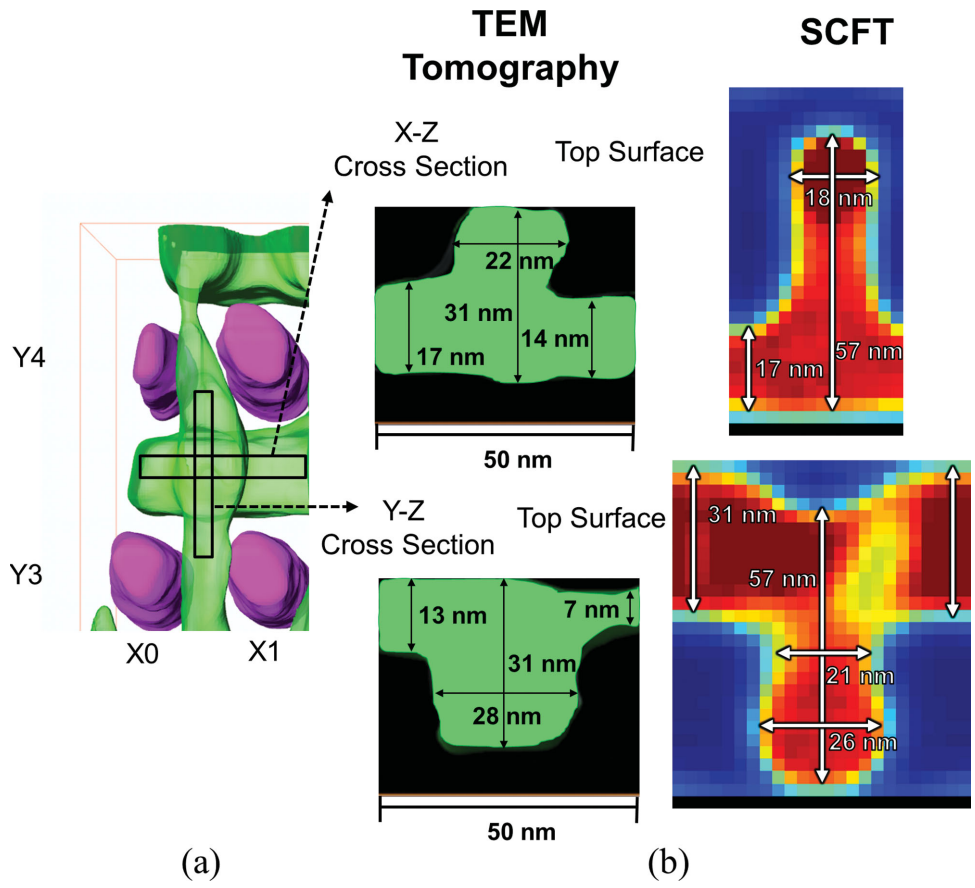


**Figure 6.** a) Location of the *x-z* and *x-y* cross section. b) TEM tomography and SCFT comparison for the connected mesh structure.

Based on the application of a PS brush to the substrate, and the lower surface energy of PDMS compared to PS, we would expect the simulation with top surface preferential to PDMS and bottom surface preferential to PS (Figure 5o) to best represent the experiment. However, the TEM data suggests that the bottom layer of cylinders was near or in contact with the substrate, though it was difficult to detect contrast between the PS and the amorphous nitride layer. Contact between PDMS and the substrate would indicate that the substrate did not have a strong affinity for PS, i.e., the actual substrate surface energy conditions were closer to neutral, possibly due to less grafting of the 11 kg/mol PS brush on the nitride substrate or poor wetting of the PS on the substrate despite the brush,[40] although carbon was present on the nitride according to X-ray photoelectron spectroscopy, see SI. (The brush grafts well to the HSQ posts making them attractive to the PS.) Additionally, the SI shows evidence that the surface wetting layer of PDMS commonly seen in annealed PS-PDMS BCPs was minimised in the solvothermal anneal process used here, i.e., the top surface was not strongly preferential to PDMS. These observations motivated the modeling of a neutral top and bottom surface shown in Figure 5m.

We note that when $\chi N = 24$ or 30 there was a large range of post heights that produced the cross-point structure (dark blue, Figure 5h) in Figure 5m. The range was smaller in Figures 5n and 5o. Cross-points were not formed for $\chi N = 18$ for any of the surface wetting situations. As expected, in the simulations with neutral top and bottom surfaces (and PS-preferential posts), the film thickness of 2.0 $L_0$ produced two layers of cylinders, whereas in the model with a PS-preferential bottom surface and PDMS top surface, a thickness of 3.0 $L_0$ produced two layers of cylinders and surface layers. In simulations with neutral surfaces, both blocks appeared at the neutral surface. From the height of each post $h_p$ and the film thickness determined from tomography data, the expected morphology around each post can be determined from the SCFT model, and is given in Table SII in the SI. SCFT predicts that the top left region of the film (HSQ posts A-C or D) would form a connected mesh structure whereas the remainder of the sample made up of shorter posts would form disconnected cylinders, based on neutral surface wetting conditions and $\chi N = 24$ or 30. Experimentally, interconnections were seen throughout the sample, indicating that interconnections formed at lower post heights than predicted by the model.

**Figure 6** shows a detailed comparison of TEM tomography and SCFT at the cross sections of a connected mesh structure in the top region (Y4 and X1 quadrant, Figure 6a) of the sample, where the SCFT calculations predicted the formation of connected mesh structures. Making a quantitative comparison is challenging because the model corresponds to equilibrium structures in the swollen film state, whereas the TEM represents the dry state. The SCFT in Figure 6 corresponds to

a film thickness of 57 nm (Figure 6b), which is based on the observed thickness of 31 nm for the dry film multiplied by a swelling ratio of nearly 2. Upon quenching, the structure is assumed to collapse in the *z*-direction as solvent is removed, reducing the out-of-plane dimensions of the microdomains and leading to elliptical cross-section cylinders as seen experimentally. Cross-sections in the *x*-*z* and *y*-*z* planes are shown. The PDMS dimensions and shape in both *x* and *y*-directions from SCFT match well to the TEM cross section measurements when the deswelling is considered, and the reduced circularity of the bottom layer PDMS is explained by the film collapsing during quenching. The differences are all within the error range of measured periodicity changes of recent in situ GISAXS measurements.[27]

We finally discuss the effect of $O_2$ RIE on the structure. Figure 3b shows the oxidized PDMS cylinders and the posts after removing the PS with oxygen. The etching produced a further shrinkage of the PDMS features in the *z*-direction, as well as some reduction in the in-plane PDMS dimensions (but not the period), particularly affecting the upper layer of cylinders. Additionally, the HSQ cylindrical posts became conical upon etching. This shows that etching preserved the overall pattern geometry in the structure, although it led to a shrinkage in the PDMS features. With these considerations, the structure of the film after drying can be deduced from its appearance after etching.

## 3. Conclusions

In summary, 3D TEM tomography enabled characterization of the 3D structure of a solvothermally annealed, templated PS-*b*-PDMS block copolymer film without staining or etching, by preparing samples on TEM grids. A direct image of the 3D templated structure without the distortions caused by etching provides valuable insight into microdomain morphology resulting from solvent anneal. Tomography demonstrated the presence of cross-point structures formed between two orthogonal layers of cylinders over the majority of the sample. The cylinder cross-sections were elliptical indicating collapse during deswelling. The results also gave indications of the surface affinity of the substrate and the air interface, based on the presence or absence of wetting layers. Etching in oxygen removed the majority PS block and oxidized the PDMS, and reduced the in-plane dimensions of the PDMS cylinders, particularly those in the upper layer. Etching also tapered the posts into truncated conical shapes. The results show that many aspects of the unetched structure can be deduced from the etched structure, but the out-of-plane microdomain dimensions are reduced by etching.

SCFT simulations of the solvent annealed sample were carried out in the strong segregation limit where the polymer is modeled in its swelled state with effective $\chi$ and $f$ resulting from solvent incorporation. A range of microdomain morphologies was obtained depending on the post height, interface wetting conditions, and values of $\chi$N and $f$. The results demonstrated interconnections in a crossbar structure over a range of post heights, $\chi$N, $f$ and surface chemistry, and the modeled geometry of a cross-point junction in the swelled film matched qualitatively with the experimental data for the dry film, taking into account the collapse of the features in the out-of-plane direction during drying. Although the agreement between SCFT and experiment is inexact, and the appropriate input parameters for the model are not known exactly for the solvent annealed situation, the results still provide a useful validation for applying SCFT to solvent annealed films. Future work with alternative dynamical models that are being developed can try to better close the gap between simulations and experiments. These experimental and theoretical methods can be applied to similar structures in the future to allow both characterization and design of templates for directed self-assembly.

## 4. Experimental Section

*Template Fabrication*: A scanning electron beam system was used to fabricate the post array of negative tone HSQ resist (Dow Corning XR-1541 2% solids). (40 ± 2) nm HSQ was spun cast (3000 RPM) on a 3 mm diameter $Si_3N_4$ TEM grid (two nitride windows of 0.1 mm × 1.5 mm) which consisted of a 50 nm thick prime $Si_3N_4$ support film acting as the window. A 125-kV acceleration voltage, 1 nA electron beam was used to expose the HSQ resist in the center region of the windows. This exposure was done by point exposure with a dwell time at each coordinate of 70 µs to 100 µs. Shortly after exposure, a 4 % NaCl/1 % NaOH by mass DI water salty-developer solution was used to develop the exposed samples for 4 min at room temperature with moderate agitation. The sample was then exposed to 2 min of DI water to remove residual developer solution and then 10 s in IPA to reduce surface capillary forces that could strain or break patterned features or the TEM grid window itself before the film was dried using $N_2$ gas. Finally, an oxygen plasma asher (50 W, 46 Pa (0.35 Torr)) was used to clean residual HSQ from the surface and harden the HSQ pattern for 2 min yielding the post pattern with post heights of (38 ± 2) nm.

*Block Copolymer Self-Assembly*: The $Si_3N_4$ substrates with HSQ posts were chemically functionalized with hydroxyl-terminated PS (11 kg mol$^{-1}$, PolymerSource) by spinning solutions of the brush then baking the samples in a vacuum oven for 16 hr at a pressure of ≈2600 Pa (≈ 20 Torr) and temperature of 170 °C. After baking, the samples were rinsed with toluene to remove unreacted brush and then dried using $N_2$ gas. 45.5 kg/mol PS-*b*-PDMS (Polymer Source, Inc. P7517-SDMS, $f_{PDMS}$ = 0.32) as 2 wt% in PGMEA solution at 272 rad·s$^{-1}$ (2650 RPM) was spun cast onto the brush-treated TEM grid.

*Solvent Annealing*: Solvothermal vapor annealing was performed on the samples using methods that produced a crossbar-like structure of PDMS cylinders from 45.5 kg/mol PS-*b*-PDMS. This is explained in previous work describing a rapid annealing system.[40] Briefly, a 5:1 by volume saturated vapor of toluene:n-heptane was prepared in an annealing chamber. Then, the TEM grid was rapidly (to prevent solvent vapor loss) placed in the environment on top of an ambient temperature resistive heater. After 4.5 min, the resistive heater was turned on and allowed to heat for 30 s from room temperature (23 ± 1) °C to (43 ± 1) °C. The heating drives out the solvent from the film and ends the annealing. Afterwards, the TEM grid is removed from the annealing chamber. Following the solvent annealing, the TEM grid was imaged directly by TEM tomography or subjected to reactive ion etching, where a 5 s $CF_4$ reactive ion etch (RIE) with power 50 W and pressure pressure 2 Pa (15 mTorr) was performed to remove any PDMS surface layer. A 22 s oxygen RIE with power 90 W and pressure 0.8 Pa (6 mTorr) immediately followed in order to oxidize the underlying PDMS cylinders and remove the surrounding PS matrix. SEM images were then obtained.

*TEM Tomography*: TEM tomography was performed on both pre- and post- reactive ion-etched, solvothermal-annealed BCP films prepared on an electron transparent $Si_3N_4$ support film. Using a TEM tomography

holder and an operating voltage of 200kV, bright-field images (with an applied constant defocus value of no higher than 3.5 μm, that will allow for theoretical resolution of at least 3 nm) were collected through a tilt range of negative 60° to positive 60° (at 5° increments from negative 45° to positive 45° and in 3° increments from 45° to 60°).[34] Beam damage can limit the quality of tomography reconstructions. The acquisition parameters were chosen to limit the total electron dose which was approximately $1 \times 10^6$ electrons/nm$^2$ for the complete tomography experiment. After acquisition it was observed that the feature sizes were unchanged compared to the initial state and therefore beam damage does not significantly affect the data. Images were recorded with 4x pixel binning, giving a $512 \times 512$ pixel array, using a charge-coupled detector (CCD). Tilt series images were corrected for spatial misalignment using cross correlation, and the tilt axis was identified using semi-automated methods in a commercial tomography reconstruction software package. Reconstruction was performed using the SIRT algorithm applied through the same software. A volume of 296 nm × 296 nm × 40 nm with a voxel size of 1 nm × 1 nm × 1 nm was reconstructed for the unetched film. As noted above, due to the discrete sampling of Fourier space and missing wedge artifacts the resolution parallel to the optic axis (z-depth) is expected to be different from the in-plane resolution in the reconstructed volume. The resolution, $\delta$, in z can be estimated from the sample thickness and maximum tilt angle as $\delta \approx t/100 \times \cos\theta_{max}$. For a thickness of 90 nm (where the transparent $Si_3N_4$ support and the unetched BCP films are 50 and 40 nm, respectively) the resolution in z is ≈ 2 nm.[41] Segmentation (thresholding) was performed manually on the reconstructed image stack to define the features to produce the surface rendering of the reconstruction through commercial tomography visualization software. Segmentation by this method introduces correlated x/y and z edge position uncertainties of ±0.15 nm and ±0.3 nm respectively, corresponding to an uncertainty in circularity of ±0.02. The resulting segmented image stacks were rotated to align the cross bar structures with the x and y axes of the reconstruction and remove a slight incline of the film. A 3 pixel (approximately 3 nm) median filter was also applied to the visualized features (surface rendering) of the image stack as a smoothing operation, consistent with the theoretical resolution limit of TEM tomography performed under these conditions. The rendered features were then measured to determine the average diameters, circularity, and heights of the template HSQ posts using slice-by-slice analysis. The PDMS cylinder average diameters and circularity were measured in the same way in the regions where the cylinders were unconnected to neighboring PDMS cylinders. In regions where the PDMS cylinders were connected, only the overall thickness was measured. For visualization, but not quantitative analysis, of the reconstructed 3D volume, smoothing was applied in the visualization software. The constrained tilt angles between ± 60° have been reported to cause an elongation errors of ≈ 1.16 in the z-direction that was predicted by the model of Kawase et al.[35] However, the study had not applied a simultaneous iterative reconstruction technique (SIRT) algorithm and therefore the elongation factor could be different. Since the HSQ posts are cylindrical, the measurement of the ellipse generated from the different tilts can provide an internal calibration for the post height prior to reconstruction and free of elongation errors. Video of the tilt series is presented in Video S4 in the SI. The trigonometry details of the calculation of HSQ post measured from tilt series images at 0° and 20° is provided in Figure S3 in the SI. From this measurement, the elongation factor of the system was calculated to be ≈ 1.07. For features below 7 nm less than 1 nm elongation will be observed, features between 8 nm and 22 nm have ≈ 1 nm of elongation. All of the measurements from TEM tomography presented in the paper besides circularity have been corrected for an elongation factor of 1.07.

## Supporting Information

Supporting Information is available from Wiley Online Library or from the author.

## Acknowledgements

The authors gratefully acknowledge support of the Semiconductor Research Corporation; the C-SPIN Center, a STARnet Center supported by MARCO and DARPA; Tokyo Electron; Taiwan Semiconductor Manufacturing Company; and the National Science Foundation. Disclaimer: Certain commercial equipment, instruments, or materials are identified in this report in order to specify the experimental procedure adequately. Such identification is not intended to imply recommendation or endorsement by the National Institute of Standards and Technology, nor is it intended to imply that the materials or equipment identified are necessarily the best available for the purpose.

Received: July 22, 2014
Revised: August 30, 2014
Published online: October 2, 2014

[1] D. P. Sanders, *Chem. Rev.* **2010**, *110*, 321–360.
[2] R. Ruiz, H. Kang, F. A. Detcheverry, E. Dobisz, D. S. Kercher, T. R. Albrecht, J. J. DePablo, P. F. Nealey, *Science* **2008**, *321*, 936–939.
[3] M. P. Stoykovich, M. Müller, S. O. Kim, H. H. Solak, E. W. Edwards, J. J. de Pablo, P. F. Nealey, *Science* **2005**, *308*, 1442–1446.
[4] S.-M. Park, X. Liang, B. D. Harteneck, T. E. Pick, N. Hiroshiba, Y. Wu, B. A. Helms, D. L. Olynick, *ACS Nano* **2011**, *5*, 8523–8531.
[5] S. B. Darling, *Prog. Polym. Sci.* **2007**, *32*, 1152–1204.
[6] M. P. Stoykovich, P. F. Nealey, *Science* **1997**, *276*, 1401–1404.
[7] X.-Y. Bao, H. Yi, C. Bencher, L. Chang, H. Dai, Y. Chen, P.-T. J. J. Chen, H.-S. P. P. Wong, IEEE Int. Electron Devices Meeting **2011**, 7.7.1–7.7.4.
[8] B. D. Terris, T. Thomson, *J. Phys. D. Appl. Phys.* **2005**, *38*, R199–R222.
[9] S. Y. Yang, I. Ryu, H. Y. Kim, J. K. Kim, S. K. Jang, T. P. Russell, *Adv. Mater.* **2006**, *18*, 709–712.
[10] E. A. Jackson, M. A. Hillmyer, *ACS Nano* **2010**, *4*, 3548–3553.
[11] P. P. Soo, B. Huang, Y.-I. Jang, Y.-M. Chiang, D. R. Sadoway, A. M. Mayes, *J. Electrochem. Soc.* **1999**, *146*, 32–37.
[12] Q. Xiao, X. Wang, W. Li, Z. Li, T. Zhang, H. Zhang, *J. Memb. Sci.* **2009**, *334*, 117–122.
[13] T. Thurn-Albrecht, J. Schotter, G. A. Kästle, N. Emley, T. Shibauchi, L. Krusin-Elbaum, K. Guarini, C. T. Black, M. T. Tuominen, T. P. Russell, *Science* **2000**, *290*, 2126–2129.
[14] A. Haryono, W. H. Binder, *Small* **2006**, *2*, 600–611.
[15] V. V. Ginzburg, J. D. Weinhold, P. Trefonas, *J. Polym. Sci. Part B Polym. Phys.* **2013**, DOI:10.1002/polb.23365.
[16] Y. Wu, G. Cheng, K. Katsov, S. W. Sides, J. Wang, J. Tang, G. H. Fredrickson, M. Moskovits, G. D. Stucky, *Nat. Mater.* **2004**, *3*, 816–822.
[17] R. J. Spontak, M. C. Williams, D. A. Agard, *Polymer* **1988**, *29*, 387–395.
[18] R. J. Spontak, J. C. Fung, M. B. Braunfeld, J. W. Sedat, D. A. Agard, L. Kane, S. D. Smith, M. M. Satkowski, A. Ashraf, D. A. Hajduk, S. M. Gruner, *Macromolecules* **1996**, *29*, 4494–4507.
[19] P. A. Midgley, E. P. W. Ward, A. B. Hungría, J. M. Thomas, *Chem. Soc. Rev.* **2007**, *36*, 1477–1494.
[20] T. Xu, A. V. Zvelindovsky, G. J. A. Sevink, K. S. Lyakhova, H. Jinnai, T. P. Russell, *Macromolecules* **2005**, *38*, 10788–10798.
[21] D. Bae, G. Jeon, H. Jinnai, J. Huh, J. K. Kim, *Macromolecules* **2013**, *46*, 5301–5307.
[22] B. E. McKenzie, F. Nudelman, P. H. H. Bomans, S. J. Holder, N. A. J. M. Sommerdijk, *J. Am. Chem. Soc.* **2010**, *132*, 10256–10259.
[23] C.-K. Chen, H.-Y. Hsueh, Y.-W. Chiang, R.-M. Ho, S. Akasaka, H. Hasegawa, *Macromolecules* **2010**, *43*, 8637–8644.

[24] K. Thorkelsson, A. J. Mastroianni, P. Ercius, T. Xu, *Nano Lett.* **2012**, *12*, 498–504.
[25] Z. Li, K. Hur, H. Sai, T. Higuchi, A. Takahara, H. Jinnai, S. M. Gruner, U. Wiesner, *Nat. Commun.* **2014**, *5*, 3247.
[26] D. F. Sunday, M. R. Hammond, C. Wang, W. Wu, R. J. Kline, G. E. Stein, *J. Micro/Nanolithogr.* **2013**, *12*, 031103.
[27] X. Gu, I. Gunkel, A. Hexemer, W. Russell, T. P. Gu, *Adv. Mater.* **2014**, *26*, 273–281.
[28] R. Gronheid, P. Rincon Delgadillo, H. Pathangi, D. Van denHeuvel, D. Parnell, B. Teik Chan, Y.-T. Lee, L. Van Look, Y. Cao, Y. J. Her, G. Lin, R. Harukawa, V. Nagaswami, L. D'Urzo, M. Somervell, P. Nealey, *Proc. SPIE* **2014**, *9049*, 904905.
[29] K G A. Tavakkoli, K. W. Gotrik, A. F. Hannon, A. Alexander-Katz, C. A. Ross, K. K. Berggren, *Science* **2012**, *336*, 1294–1298.
[30] G. H. Fredrickson, *The Equilibrium Theory of Inhomogeneous Polymers* Series: International Series of Monographs on Physics (Vol. 134), Oxford University Press Oxford, UK **2006**.
[31] G. H. Fredrickson, V. Ganesan, F. Drolet, *Macromolecules* **2002**, *35*, 16–39.
[32] R. A. Mickiewicz, J. K. W. Yang, A. F. Hannon, Y.-S. Jung, A. Alexander-Katz, K. K. Berggren, C. A. Ross, *Macromolecules* **2010**, *43*, 8290–8295.
[33] K G A. Tavakkoli, K G A. Hannon, K. W. Gotrik, A. Alexander-Katz, C. A. Ross, K. K. Berggren, *Adv. Mater.* **2012**, *24*, 4249–4254.
[34] J. Frank, *Electron Tomography: Methods for Three-Dimensional Visualization of Structures in the Cell*, Springer, Berlin, **2008**, 470.
[35] N. Kawase, M. Kato, H. Nishioka, H. Jinnai, *Ultramicroscopy* **2007**, *107*, 8–15.
[36] T. Nose, *Polymer* **1995**, *36*, 2243–2248.
[37] Y. S. Jung, C. A. Ross, *Nano Lett.* **2007**, *7*, 2046–2050.
[38] J. G. Kennemur, L. Yao, F. S. Bates, M. A. Hillmyer, *Macromolecules* **2014**, *47*, 1411–1418.
[39] S. P. Paradiso, K. T. Delaney, C. J. García-Cervera, H. D. Ceniceros, G. H. Fredrickson, *ACS Macro Lett.* **2014**, *3*, 16–20.
[40] H. Lee, H. Ahn, S. Naidu, B. S. Seong, D. Y. Ryu, D. M. Trombly, V. Ganesan, *Macromolecules* **2010**, *43*, 9892–9898.
[41] K. W. Gotrik, C. A. Ross, *Nano Lett.* **2013**, *13*, 5117–5122.
[42] P. A. Midgley, R. E. Dunin-Borkowski, *Nat. Mater.* **2009**, *8*, 271–280.